https://doi.org/10.5194/essd-2026-576
Preprint. Discussion started: 31 August 2026

Open Access Earth System Science Data Discussions

Updating the ESA Earth System Model for Future Gravity Mission Simulation Studies: ESA ESM 3.0

Linus Shihora[1], Laura Jensen[1], Eva Boergens[1], Volker Klemann[1], Robert Dill[1], Ingo Sasgen[2], Bert Wouters[3], Marius Schlaak[4], Jeanne Sauber-Rosenberg[5], Shin-Chan Han[6], Yoshiyuki Tanaka[7], Carla Braitenberg[8], Muhammad Tahir Javed[8], Gerardo Maurizio[8], Hugo Lecomte[9], Andrey Babeyko[1], Niels Hovius[1], and Henryk Dobslaw[1]

[1]GFZ Helmholtz Centre for Geosciences, Potsdam, Germany
[2]Alfred-Wegener-Institut, Helmholtz-Zentrum für Polar- und Meeresforschung, Bremerhaven, Germany
[3]TU Delft, Civil Engineering, Geoscience and Remote Sensing, Netherlands
[4]Technical University of Munich, Astronomical and Physical Geodesy, Munich, Germany
[5]Geodesy and Geophysics Laboratory, NASA Goddard Space Flight Center, Greenbelt, MD, USA
[6]Ohio State University, School of Earth Sciences, Columbus, OH, United States
[7]University of Tokyo, Department of Earth and Planetary Science, Tokyo, Japan
[8]Dipartimento di Scienze della Terra, Università di Trieste, Via Weiss 1, 34100 Trieste, Italy
[9]Finnish Geospatial Research Institute, National Land Survey of Finland

Correspondence: Linus Shihora (linus.shihora@gfz.de)

Abstract. The ESA Earth System Model (ESA ESM) provides a synthetic data set of the time-variable global gravity field that includes realistic mass variations in the atmosphere, oceans, terrestrial water storage, continental ice sheets, and the solid Earth on a wide range of spatial and temporal frequencies.

We here present the details of the newly released version 3.0 of the ESA ESM which has been updated to reflect the increased capabilities of future satellite gravimetry missions and is designed to be used as a source input model in closed loop simulation studies. The changes to the previous ESA ESM 2.0 include the utilization of a small ensemble of co- and post-seismic earthquake signals, an updated GIA model, additional mass balance signals from previously not considered Arctic glaciers, sub-monthly surface-mass balance changes and a more realistic representation of ice sheet dynamics. Extreme hydrometeorological events as well as climate-driven and anthropogenic impacts on continental water storage are represented through an update of the hydrological component. Additionally, the ESM separately includes ocean bottom pressure variations along the western slope of the Atlantic, representing variations in the meridional overturning circulation as a critically important component of the interactively coupled global climate system. ESA ESM 3.0 is available with 6-hour resolution from January 2007 until December 2020 as separate layers representing the respective dynamic processes considered. It is augmented with synthetic error time series for atmosphere and ocean as well as hydrology to facilitate stochastical modelling of residual background model errors.

The updated ESA ESM 3.0 is available under:

Shihora, Linus; Klemann, Volker; Jensen, Laura; Dill, Robert; Sasgen, Ingo; Wouters, Bert; Sauber, Jeanne; Han, Shin-Chan; Tanaka, Yoshiyuki; Braitenberg, Carla; Javed, Muhammad Tahir; Maurizio, Gerardo; Lecomte, Hugo; Babeyko, Andrey; Hov-

https://doi.org/10.5194/essd-2026-576
Preprint. Discussion started: 31 August 2026

Open Access Earth System Science Data Discussions

ius, Niels; Dobslaw, Henryk (2026): The ESA Earth System Model 3.0. GFZ Data Services. https://doi.org/10.5880/GFZ.UEOS.2026.001

1 Introduction

The time-variable gravity field has been monitored by satellite gravimetry missions such as GRACE and GRACE Follow-On for now over two decades. Through better instruments, a continuously extending time-series and refined processing strategies, the resulting monthly gravity fields continue to be applied to a variety of geophysical applications (Chen et al., 2022). Given the projected end of the GRACE-FO mission, one of the major objectives for future satellite gravimetry missions is the continuity of the time-series without any gaps, and work towards new missions is already ongoing. In mid-2026, GRACE-Continuity (GRACE-C) has passed the Critical Design Review and is expected to launch in 2028, while the Next Generation Gravity Mission (NGGM) is being prepared by the European Space Agency (ESA) with a tentative launch in 2033. Together, GRACE-C and NGGM will constitute the Mass change And Geosciences International Constellation (MAGIC) and feature two satellite pairs in a Bender-type constellation (Bender et al., 2008), thereby offersing the prospect of resolving much smaller spatial scales than previously accessible from GRACE alone (Pail et al., 2015).

In preparation of any future gravity mission, end-to-end simulation studies for a wide variety of geophysical applications are necessary (e.g., Daras et al., 2023; Kusche et al., 2025). These simulation studies are commonly based on simulated satellite orbits using a source model of global mass variations. Based on these orbits, a time-series of global gravity field solutions is then retrieved considering approaches towards e.g. mitigation of temporal aliasing and filtering strategies. Finally, surface mass variations are calculated which can be compared to the variations in the input source model applied in the initial orbit simulation step. Up to now, the ESA Earth System Model (ESA ESM) 2.0 (Dobslaw et al., 2015) has been the standard input source model for such simulations. It represents mass variations in atmosphere (A), ocean (O), hydrology (H), ice-sheets and glaciers (I) as well as the solid earth (S) split into individual layers of Stokes coefficients. Additionally, it provides an uncertainty estimate of the atmosphere and ocean coefficients which can be used for a realistic representation of de-aliasing effects in simulations (Dobslaw et al., 2016).

With the increased capabilities of future satellite gravimtery missions such as MAGIC, preparatory simulation studies – and consequently also the ESA ESM source model – must include appropriate geophysical target signals such that mission requirements and processing strategies can be reliably tested. We therefore present here the work towards a new version 3.0 of the ESA ESM. This includes updates of the previously existing AOHIS layers as well as three new layers representing a sea-level variations for mass conservation (B), a separate layer with various earthquakes (E), as well as a layer representing regionally confined processes (D) such as ocean bottom pressure (OBP) anomalies along the western boundary of the Atlantic Ocean representing variations in the overturning circulation or erosion of sediments over river basins with corresponding ma-

https://doi.org/10.5194/essd-2026-576
Preprint. Discussion started: 31 August 2026

Open Access Earth System Science Data Discussions

rine deposition.

In the following, we dedicate a subsection to each of the layers of the ESA ESM 3.0 (Sec. 2.1 – 2.8). Initial simulations are assessed on coefficient level in Sec. 3 and results are compared to observed monthly gravity solutions from GravIS in Sec. 4. We highlight important technical aspects as well as data access in Sec. 5, before concluding the article in Sec. 6.

2 The ESA Earth-System Model 3.0

In the following section we give details on each of the layers of the new ESA ESM 3.0. While the Subsections 2.1 to 2.5 refer to updated layers, Subsections 2.6 to 2.8 give details on newly introduced layers.

2.1 Atmosphere Layer

The ESA ESM A-layer represents the mass variations in the atmosphere on sub-daily to inter-annual time-scales. For the new version 3.0, we use the latest ERA5 reanalysis data from the European Centre for Medium-range Weather Forecasts (ECMWF) (Hersbach et al., 2020).

Over land, the A-layer consists of atmospheric surface pressure anomalies, while over the oceans only the static and uniform contribution of surface pressure to ocean bottom pressure (OBP) is included. In addition, the layer includes the much smaller contribution of density anomalies in the upper atmosphere for the whole globe, calculated through a vertical integration of the atmospheric density as given on the terrain-following 137 levels. Atmospheric tidal signals are estimated and subsequently subtracted as described by Balidakis et al. (2022) using the full hourly resolution of ERA5. The atmospheric component is thus compatible with the current release RL07 of the Atmosphere and Ocean De-Aliasing Level-1B (AOD1B) Product (Shihora et al., 2022a). Unlike AOD1B, however, the ESA ESM 3.0 does not make a transition to operational numerical weather prediction data from ECMWF and, for the sake of consistency, uses ERA5 for the entire period sub-sampled to 6-hourly epochs.

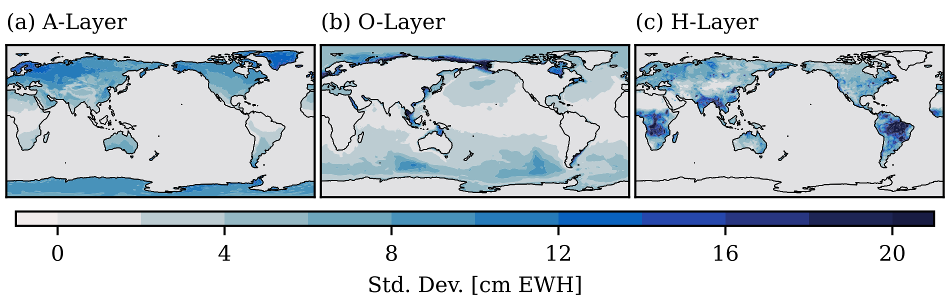

Figure 1. Standard deviation of the ESA ESM 3.0 A, O and H-layers in (a) – (c) respectively.

https://doi.org/10.5194/essd-2026-576
Preprint. Discussion started: 31 August 2026

2.2 Ocean Layer

In line with the updated atmospheric layer, the new O-layer of the ESA ESM 3.0 represents oceanic mass variations on sub-daily to inter-annual time-scales. It is based on a numerical simulation with the Max-Planck-Institute for Meteorology Ocean Model (MPIOM, Jungclaus et al. (2013)) using its TP10L40 configuration with a 1° tripolar Arakawa-C grid and 40 vertical z-levels. The model is forced using atmospheric ERA5 reanalysis data including surface pressure forcing and includes the full feedback from self-attraction and loading (Shihora et al., 2022b). We extract hourly OBP fields, estimate and remove atmospherically induced tidal signals, and artificial fluctuations in the total ocean mass due to the Boussinesq approximation are corrected (Greatbatch, 1994). Finally, the OBP anomalies are subsampled to 6-hourly epochs.
In contrast to the previous version 2.0 of the ESA ESM, we explicitly note that the oceanic layer in ESM 3.0 is mass conserving. Instead, the change in sea-level is provided in a separate layer described in Subsection 2.6.

2.3 Hydrology Layer

For the updated H-layer, we use a dedicated hydrological simulation with the OS LISFLOOD model (Van Der Knijff et al. (2010), https://ec-jrc.github.io/lisflood-model/) which has previously been shown by Jensen et al. (2025) to better represent variations in terrestrial water storage (TWS) compared to LSDM used in the previous ESA ESM version. The quasi-global (to 60° S) 0.05° simulation uses ERA5 atmospheric forcing consistent with the A and O-layers and employs the 'LISFLOOD static and parameter maps for GloFAS v1.0' provided by the Joint Research Centre (JRC) of the European Commission (Choulga et al., 2023). The model explicitly considers 463 lakes and 667 reservoirs and features an anthropogenic groundwater abstraction module.
In contrast to the standard setup, we modified soil-depth maps to account for spurious linear trends in earlier simulations and correct the snow module for erroneous snow accumulation (Jensen et al., 2025). Daily TWS fields are extracted by combining the soil, groundwater, snow and surface water components. In order to avoid double-counting of the contributions, we disregard the snow contributions in glaciated regions which are included in the I-layer (Sec. 2.4). Lastly, we match the temporal resolution of the other layers by interpolating linearly to 6-hourly epochs and apply a 2D Gaussian filter with a 50 km radius in order to minimize the Gibbs effects arising from the transformation into Stokes coefficients.

2.4 Ice Layer

To represent the cryospheric mass variations in the I-layer, we combine individual simulations for Greenland, Antarctica, nine glacier regions and estimates of mass change signals in the arctic permafrost.

For Greenland and Antarctica, signals are based on daily surface mass-balance (SMB) variability from the regional climate model MAR v3.12 combined with long-term ice-dynamic trends and accelerations derived from ISSM from ISMIP6. The combined signal is then calibrated against GRACE and GRACE-FO data from 2007-2021.

https://doi.org/10.5194/essd-2026-576
Preprint. Discussion started: 31 August 2026

Glacier mass changes for the Arctic regions (Alaska, Arctic Canada, Iceland, Svalbard, Russian Arctic) are based on daily output from the RACMO (Noël et al., 2018, 2020, 2022) and MAR (Fettweis and Grailet, 2024; Fettweis et al., 2013) regional climate models. Since the models only provide surface mass balance and observations of ice discharge are very limited in space and time, the model output is bias-corrected so that the data reproduces the observed mass loss in the GRACE period. Outside the Arctic, RACMO model data was used for the ice fields in Southern Patagonia at daily resolution (Noël et al., 2025). For the regions of Alaska, High Mountain Asia and the European Alps no model data with the required spatio-temporal resolution were available. Instead, the regions are represented by consecutive five-yearly high-resolution elevation change estimates based on stereophotogrammetry (Hugonnet et al., 2021) converted to mass changes using a reference density of 850 kg m^{-3}.

We also include permafrost signals, which are represented only as a linear mass-change trend modeled from 1960 – 2020 which is projected and interpolated onto a regular 0.25° grid.
All individual components are interpolated linearly to 6-hourly epochs, combined to a single grid and also smoothed using a 50km Gaussian filter in order to minimize Gibbs effects.

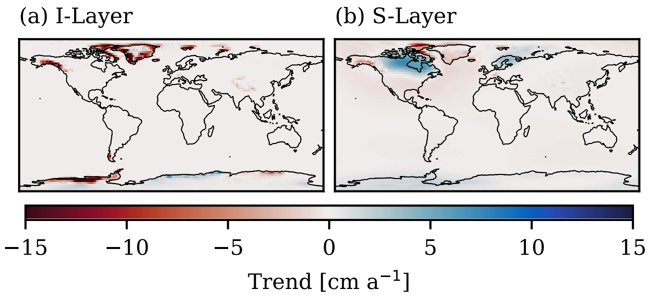

Figure 2. Trend in cm EWH per year of the ESA ESM 3.0 I (a) and S-layers (b).

2.5 Solid Earth Layer

The last of the updated layers, represents the mass-change signals in the solid earth. It combines glacial isostatic adjustment (GIA) contributions from the last glacial cycle, signals from the Little Ice Age (LIA) and gravitaional signals from pressure changes at the core-mantle boundary (CMB).

The GIA component is modelled by applying the Viscoelastic Lithosphere and MAntle model VILMA (Klemann et al., 2008). The model consistently considers the effects of gravity, rotation and deformation of the Earth (GRD, Gregory et al. (2019)) while solving the linear viscoelastic and incompressible self-gravitating continuum under consideration of the sea level equation with moving coastlines and floating ice (Hagedoorn et al., 2007).
As forcing we consider the glaciation history ICE6G_C (Peltier et al., 2015). In contrast to the associated 1D viscosity structure

https://doi.org/10.5194/essd-2026-576
Preprint. Discussion started: 31 August 2026

vm5a, the 3D viscosity structure v0.4-s16 is used (Bagge et al., 2021; Albrecht et al., 2024). It is based on seismic tomography and geodynamic constraints (Steinberger, 2016) and served as a more realistic representation of the Earth responding to glacial loading.

For the inclusion of the LIA induced signals, we force VILMA with a reconstruction of glacial mass change from the Open Global Glacier Model (OGGM, Maussion et al. (2019, 2022)) with a one-dimensional low-viscosity earth structure with an asthenosphere viscosity of 10^{19} Pa s and a lithosphere thickness of 40 km.

As a second new contribution, the S-layer also considers gravitational changes induced by pressure changes at the core-mantle boundary simulated using the geomagnetic model AR-3 (Gillet et al., 2024) and by potential Love numbers from Dumberry and Mandea (2022). The signals are included on monthly time-scales up to degree and order 10. Nonetheless, all solid Earth signals are combined on a coefficient leven, interpolated linearly to 6-hourly epochs and extended to degree and order 180.

2.6 Sea-Level Layer

In contrast to ESA ESM 2.0, manometric sea-level changes are not part of the O-layer but considered in the dedicated B-layer. This layer balances changes in the atmosphere, hydrology and cryosphere, i.e. the layers which are not mass-conserving themselves. As a result, it ensures mass conservation for the combined layers of the ESA ESM 3.0.
As formulated by Farrell and Clark (1976) and discussed further in Gregory et al. (2019), changes in the hydrospheric surface load affect the gravity, rotation and deformation of the Earth and require solving the sea-level equation. For the B-layer, we use the iterative approach described by Tamisiea et al. (2010) using the combination of the A, H and I-layers as inputs at their full resolution. The result is a global 6-hourly time-series of sea-level variations which compensates the mass variations over the continents on both short time-scales as well as long-term trends.

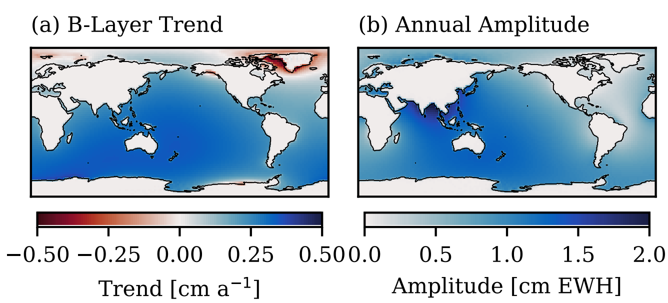

Figure 3. Linear trend in cm a^{-1} (a) and amplitude of the annual signal (b) of the ESA ESM 3.0 B-layer.

https://doi.org/10.5194/essd-2026-576
Preprint. Discussion started: 31 August 2026

Table 1. Earthquake events included in the ESA ESM 3.0 E-layer. Events are artificially placed in the second year (2008) of the ESM with one event in the middle of each month ordered by magnitude.

Earthquake	Magnitude	Location	Original Date	ESM 3.0 Epoch
Sumatra-Andaman	9.2	3.35°N, 94.8°E	Dec 26th, 2004	Jan 16th, 2008
Tohoku-Oki	9.0	38.3°N, 142.4°E	Mar 11th, 2011	Feb 14th, 2008
Maule	8.8	35.9°S, 286.6°E	Feb 27th, 2010	Mar 16th, 2008
Nias-Simeulue	8.6	1.53°N, 97.1°E	Mar 28th, 2005	Apr 15th, 2008
Indian Ocean	8.6	1.80°N, 92.3°E	Apr 11th, 2012	May 16th, 2008
Bengkulu	8.5	3.97°S, 100.9°E	Sep 12th, 2007	Jun 15th, 2008
Sea of Okhotsk	8.3	54.6°N, 153.7°E	May 24th, 2013	Jul 16th, 2008
Kuril Islands	8.3	48.6°N, 154.8°E	Nov 15th, 2006	Aug 16th, 2008
Papua New Guinea	8.1	5.6°S, 154.3°E	Jan 22nd, 2017	Sep 15th, 2008
Samoa	8.1	15.9°S, 187.3°E	Sep 29th, 2009	Oct 16th, 2008
Macquarie	8.1	49.5°S, 161.5°E	Dec 24th, 2004	Nov 15th, 2008
Peru	7.9	5.81°S, 75.2°W	May 26th, 2019	Dec 16th, 2008
Kahramanmaraş	7.8	38.8°N, 37.6°E	Feb 6th, 2023	Jan 16th, 2009
Portugal	7.8	36.0°N, 10.5°W	Feb 28th, 1969	Feb 14th, 2009
Amorgos	7.7	36.7°N, 25.7°E	Jul 9th, 1956	Mar 16th, 2009

2.7 Earthquake Layer

In order to assess the ability of future satellite gravimetry missions to monitor fast and slow gravity changes associated with large earthquakes, we explicitly consider 15 events with different characteristics and at different locations in the E-layer of the ESA ESM 3.0. In contrast, the previous version of the ESA ESM only includes the co- and post-seismic signals from the Sumatra-Andaman earthquake. These 15 events can be divided into four groups with different modelling approaches.

The first group of nine events consists of selected events from the GRACE and GRACE-FO era. These include the 2004 M_w 9.2 Sumatra-Andaman, 2005 M_w 8.6 Nias-Simeulue, 2006/7 M_w 8.3 Kuril, 2007 M_w 8.5 Bengkulu, 2009 M_w 8.1 Samoa-Tonga, 2010 M_w 8.8 Maule, 2011 M_w 9.0 Tohoku-Oki, 2012 M_w 8.6 Indian Ocean (Wharton Basin), and 2013 M_w 8.3 Sea of Okhotsk earthquakes. Co-seismic (elastic) and post-seismic (viscoelastic) geopotential changes were modelled using the elastic and viscoelastic normal mode computations with the earthquake source and rheology parameters refined by the GRACE and GRACE-FO data. The method is an extension of Han et al. (2013) to account for the viscoelastic Earth deformation.

For the seismically very active area of Japan, we adopt a more detailed modelling approach that describes explicitly a sequence

https://doi.org/10.5194/essd-2026-576
Preprint. Discussion started: 31 August 2026

of tectonic events and the associated non-linear changes in post-seismic deformations. Earthquakes from the ISC-GEM catalogue (https://www.isc.ac.uk/iscgem/download.php) were extracted for the period from January 21, 1906, to April 15, 2016, within the region bounded by longitudes 125°E–160°E and latitudes 20°N–55°N, and with moment magnitudes $M_w \geq 7.0$. The total number of the selected earthquakes is 109 (only the Tohoku event is explicitly listed in Tab. 1). All sources, including the 2011 M_w 9.0 Tohoku earthquake, were treated as point sources in the simulations. Cumulative effects of co- and post-seismic gravity changes were calculated.

Third, we include co-seismic and post-seismic gravity changes related to the M_w 7.8 Kahramanmaraş earthquake in 2023. We perform forward modeling to estimate coseismic and postseismic gravity changes, geoid variations, and surface displacements induced by fault dislocations using the QSSPSTATIC code (Wang et al., 2017) using fault parameters from the U.S. Geological Service.

Lastly, in order to assess the potential observability of tectonic events in Europe, we also include two historically large events. The selected European earthquakes are in seismically active, near shore regions with probable significant vertical land motion. Because these events are offshore, the gravimetric change measurements could provide unique information beyond the constraints provided by continuous GPS and InSAR. For the 1969 Portugal earthquake (M_w 7.8), we simulate a thrust with a strike-slip component of faulting. Note, that the 1969 event was probably a complex double event with an initial deeper event that was dominantly thrust followed by a shallower event that was dominantly strike-slip. For our initial modeling, we used the simple centroid solution (Sauber et al., 2025). We also simulate the predominantly normal faulting 1956 Amorgos earthquake (M_w 7.7) to complete the ensemble.

In addition to the co- and post-seismic gravity variations due to the earthquakes, we also include the gravitational impact due to trans-ocean tsunami propagations. The 2004 Sumatra-Andaman and 2011 Tohoku-Oki tsunami waves were simulated using the GFZ tsunami generation and propagation code easyWave. easyWave is a computationally efficient implementation of the linear shallow water model on a staggered finite difference grid. We note that, being primarily designed for the rapid tsunami early warning, the linear model does not represent the dissipation terms which may lead to some overestimation of the tsunami wave, especially after numerous coastal reflections. We also note that 6-hourly temporal resolution with subsequent linear interpolation to intermittent epochs does not properly represent the progression of tsunami waves across the ocean basins. However, the chosen implementation will allow us to test the general ability of future missions to capture such occasional effects. For detailed studies, source models with much higher resolution (or alternative interpolation routines that take into account the travel direction of the waves) would be needed. For the Sumatra-Andaman event, two epochs are provided, whereas for the Tohoku-Oki event we deliver three epochs, since it takes more time for the wave to traverse the Pacific basin.

To combine all individual signal components into the final E-Layer of the ESM 3.0, we initially augment all Stokes coefficients up to degree and order 180. In order to minimise the effects of Gibbs ringing due to the steep gradients / steps, we apply a cosine taper to the Stokes coefficients starting from degree 90 as in Han et al. (2024). As the individual post-seismic deformation signals are given with a non-uniform sampling, we interpolate all events to a 6-hourly resolution and shift the event

https://doi.org/10.5194/essd-2026-576
Preprint. Discussion started: 31 August 2026

Open Access Earth System Science Data Discussions

from the original (i.e. real) epoch to the epoch given in Tab. 1. The earthquakes are artificially shifted towards the beginning of the time-series in order to allow for a long time-series of post-seismic deformations to be included.

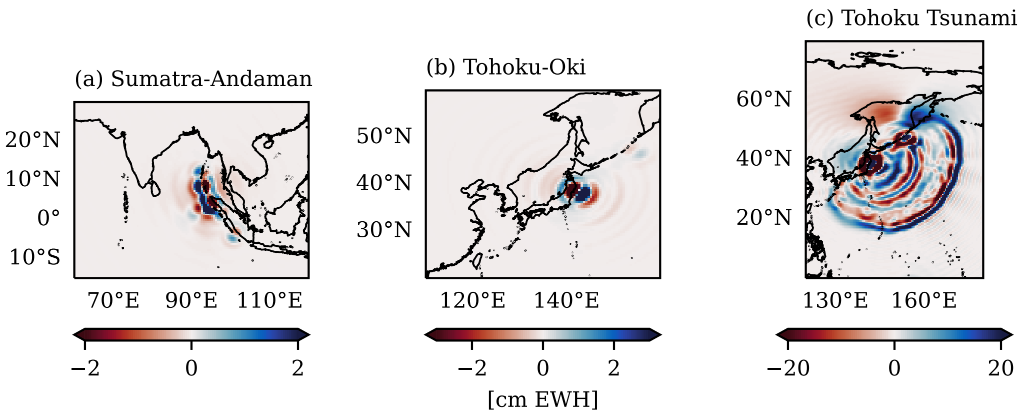

Figure 4. Selected signals in cm EWH from the ESA ESM 3.0 E-layer. (a) shows the gravity change from the Sumatra-Andaman earthquake, (b) from the Tohoku-Oki earthquake and (c) the first epoch of the included tsunami data following the Tohoku event.

2.8 AMOC & Sedimentation Layer

In the newly developed D-layer, we combine two regional target signals: (a) regional OBP variations at the western boundary of the Atlantic which are indicative of changes in the overturning and (b) regional trend estimates of sediment erosion over river basins and the subsequent marine deposition. While the two signal sources are not strictly related, they do not interfere which each other and require similar corrections and are thus combined into a single layer.

Changes in the Atlantic Meridional Overturning Circulation (AMOC) are, under the geostrophic approximation, given by the difference in bottom pressure between the eastern and western boundary of the Atlantic (Roussenov et al., 2008). As highlighted by Bingham and Hughes (2008), variations in the meridional transports can, to a good degree, be inferred through measurements of the western boundary pressure alone. To include AMOC related OBP anomalies in the ESA ESM, we generate a synthetic dataset using the regional ocean general circulation model VIKING20X (Madec et al., 2023) based on NEMO3.6 and LIM2 (Fichefet and Maqueda, 1997) provided by GEOMAR. Within the model run, we have access to daily 3D velocity fields as well as computed OBP. Two time-series of meridional transport are generated for the North and South Atlantic by integrating the velocities between 25° N – 40° N (20° S – 33° S) and 1000 m – 3000 m (1100 m – 3000 m) and applying a 5-year high-pass filter. A regression of the meridional transport time-series to ocean bottom pressure is then performed for each grid point along the western boundary of the North and South Atlantic in the corresponding latitude range. The resulting scale factor at each grid point are applied to the model-based true meridional transport anomalies to create the synthetic OBP data. The synthetic OBP data then combines the temporal behavior of the model transports with the correct signal strength

https://doi.org/10.5194/essd-2026-576
Preprint. Discussion started: 31 August 2026

of the OBP anomalies, but do not contain any other signals from ocean dynamics. The two OBP regions are then extracted, combined and a uniform layer of mass is added to the rest of the global oceans in order to balance the regional AMOC-related OBP changes and ensure mass conservation. For a more detailed description and assessment of this approach, we refer to Shihora et al. (2025). We note, however, that the inclusion of the OBP signals in the D-layers entails several choices which should be considered in subsequent simulation studies. For one, the application of a 5-year high-pass filter means that the study of long-term signals and trends is not readily possible. The choice of the cut-off frequency is mainly driven by the nominal mission lifetimes of satellite gravimetry, which is 5 years. This is especially relevant in the case of MAGIC, which relies on the combined operation of two satellite pairs with launch dates multiple years apart. Since the long-term evolution of the overturning is of great interest, simulation studies focusing on these time-scales may need a revised D-layer input in the future. Additionally, we note that there are signals in the O-layer of the ESM which will correlate with the transport related signals of the D-layer, since there is no dedicated filtering of the O-layer to avoid overlap. Simulation studies should therefore only retrieve the HISBED signal and not the AO component when focusing on the AMOC.

A unique feature of satellite gravimetry is its ability to detect mass changes regardless of their surface exposure. An application where this feature would be of great value is the measurement of river sediment discharge into the oceans which is currently only sparsely constrained from in-situ measurements, especially in areas of marine deposition. Several previous studies (Mouyen et al., 2018; Chang et al., 2019; Li et al., 2022) have focused on this particular application with the currently available GRACE/-FO data. Results obtained were rather mixed and often do not match with in situ estimates (possibly due to residual errors in the gravity data), or do not have the spatio-temporal resolution required to clearly distinguish between marine and continental signals. Consequently, including appropriate target signal estimates into the ESM 3.0 and thus in future mission simulations may help to develop processing strategies and refine future mission requirements. The ESM 3.0 D-Layer thus includes long-term trend estimates of continental erosion and marine deposition for five selected regions including Amazon, Ganges, Yangtze, and Yellow River. Additionally, we include mass change trends associated with retrogressive thaw slumps on Banks Island in the Canadian Arctic (Nitze et al., 2025).

For each of the river basins we assume a spatially homogeneous erosion trend over the entire catchment using the values given in Tab. 2 provided by Mouyen et al. (2018). For the Yellow River, however, we rely on the work by Tu et al. (2025), a assume the accumulation of sediments at the locations of the Xiaolangdi, Wanjiazhai and Sanmenxia reservoirs with a rate of 0.1 Gt a^{-1}. For the marine deposition, contours over the oceans are defined based on Fig. 2 of Mouyen et al. (2018) for the Amazon, Ganges, and Yangtze, while again relying on (Tu et al., 2025, Fig. 9) for the Yellow River. For the Yangtze and Yellow River, marine deposition is assumed as spatially uniform within the contour. For the Amazon and Ganges River, instead, a gradient using a Gaussian taper is applied to the deposition rates. The total amount of marine deposition is based on an assumed density of 2500 kg m^{-3} and considers the fact that sea-water is displaced. This results in the values given in Tab. 2 on the right. As a result, the mass change over the ocean is smaller than the total amount of erosion over the river basin. In order to account for the conservation of the total mass, any missing mass, i.e. the amount of displaced sea-water, is spread out homogeneously over the global ocean domain. For the representation of retrogressive thaw slumps on Banks Island, a spatially

https://doi.org/10.5194/essd-2026-576
Preprint. Discussion started: 31 August 2026

Table 2. Assumed sediment discharge rates for individual regions in the ESM 3.0 D-Layer. The sediment discharge represents the mass of the sediment transported into the ocean per year. The marine regional mass change represent the amount of mass that is added to the surroundings of the river mouth considering that the sediment displaces sea-water (assuming a sediment density of 2500 kg m^{-3}). For Banks Island, mass is spread out over entire ocean domain, while for the Yellow River part of the sediments are accumulated along the path of the river at the location of three artificial reservoirs.

Region	Sediment Discharge [Gt a^{-1}]	Marine Regional Mass Change [Gt a^{-1}]
Amazon River	0.8	4.7
Banks Island	0.5	-
Ganges River	1.0	5.9
Yangtze River	0.5	0.295
Yellow River	0.1	0.059

uniform mass change of -0.5 Gt a^{-1} is assumed for the area of Banks Island based on Nitze et al. (2025). The corresponding mass increase is spread homogeneously over the entire ocean domain to ensure mass conservation.

We recall that the regional sediment mass change rates are, in contrast to other components of the ESM, not based on dedicated simulations but rather derived from empirical estimates. These signals should thus be considered as a first estimate of marine deposition rates and may require a more detailed approach in the future.

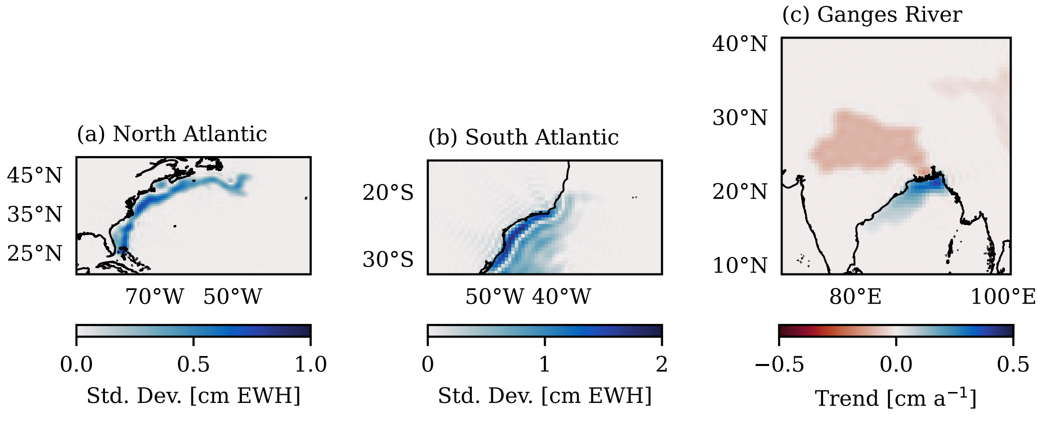

Figure 5. Standard deviation of the ESA ESM 3.0 D layer in the North (a) and South (b) Atlantic representing the synthetic OBP data related to changes in the overturning circulation. (c) shows the trend signal in cm a^{-1} from erosion in the Ganges river basin and associated marine deposition.

https://doi.org/10.5194/essd-2026-576
Preprint. Discussion started: 31 August 2026

Open Access Earth System Science Data Discussions

3 Assessment with Satellite Simulations

In the following, the ESM 3.0 is evaluated in terms of performance relative to its predecessor, the ESM 2.0. To assess the suitability of the new layers, long-term simulations have been performed over the respective periods of the ESMs: 1995-2006 (ESM 2.0) (Schlaak et al. 2026) and 2007-2020 (ESM 3.0).

The simulation setup accounts for future satellite-to-satellite tracking missions, such as GRACE-C and MAGIC. For the on-board instruments, noise assumptions from Schlaak and Pail (2025) are considered for the laser ranging instruments and accelerometers. To account for de-aliasing background model errors, non-tidal model errors are considered (Dobslaw et al., 2016; Shihora et al., 2024), as well as tidal background model errors in the form of ocean tide model differences (EOT11a (Savcenko et al., 2012) and GOT4.7 (Ray, 1999)). The gravity field retrieval is performed using the acceleration approach (Schlaak et al., 2022; Murböck, 2015) to produce monthly time-variable gravity models.

The target layers for the simulations and the reference in this comparison are HIS (for ESM 2.0) and HISBED (for ESM 3.0) averaged in monthly solutions. In the forward modelling, the target signals and non-tidal errors differ between the ESM 2.0 and ESM 3.0. The observation system, including the sampling distribution (ground tracks) and instrument noises, remains the same in this comparison. The residuals from 12 years of ESM 2.0 and 14 years of ESM 3.0 are compared by evaluating their degree amplitudes in Equivalent Water heights (EWH).

As can be seen in Figure 6, the two models show a comparable magnitude of the time variable gravity signal globally, but the ESM 3.0 exhibits a wider variation between the months. While the mean variance along the spherical harmonic spectrum is 0.76 cm EWH for the ESM 2.0, the mean variance doubles to 1.55 cm EWH in the ESM 3.0. The wider spread of ESM 3.0 is expected from the more dynamic H- and I-layer in the forward modelling. In terms of mission performance (Figure 6), the two ESMs show comparable results across the considered mission constellations. For a single-pair mission, GRACE-C-like, the signal-to-noise ratio of one for monthly solutions is reached on average at degree 32 with ESM 2.0 and at degree 38 with ESM 3.0. The slightly better average performance in ESM 3.0 stems from the lower error rates of the improved background models that accompany the ESM 3.0 compared to the AOerr (Dobslaw et al., 2016), which accompanies the EMS2.0. A similar relative improvement is visible in the double-pair (Magic-like) residuals, where the signal-to-noise ratio of one is reached at degree 65 for ESM 2.0 and 70 for ESM 3.0. The slightly larger spread in the residuals between monthly solutions in the ESM 3.0 is directly related to the greater variability in the magnitudes of the reference signals.

Overall this comparison shows, that the ESM 3.0 is a suitable model for satellite gravity simulation studies, which, given its more complex modeling of the different Earth system compartments, allows more detailed studies of the science impact of future mission constellations.

4 Comparison of L3 Simulation Output with GraviS

We also compare the simulated Level-2 (L2) data from a polar-pair simulation based on the ESM 3.0 with the operationally processed GRACE and GRACE-FO TWS products as available via GravIS (Boergens et al., 2020). These operational products are based on the COST-G L2 dataset (Meyer et al., 2025). From the polar-pair simulation generated within the SING consortium

https://doi.org/10.5194/essd-2026-576
Preprint. Discussion started: 31 August 2026

Open Access Earth System Science Data Discussions

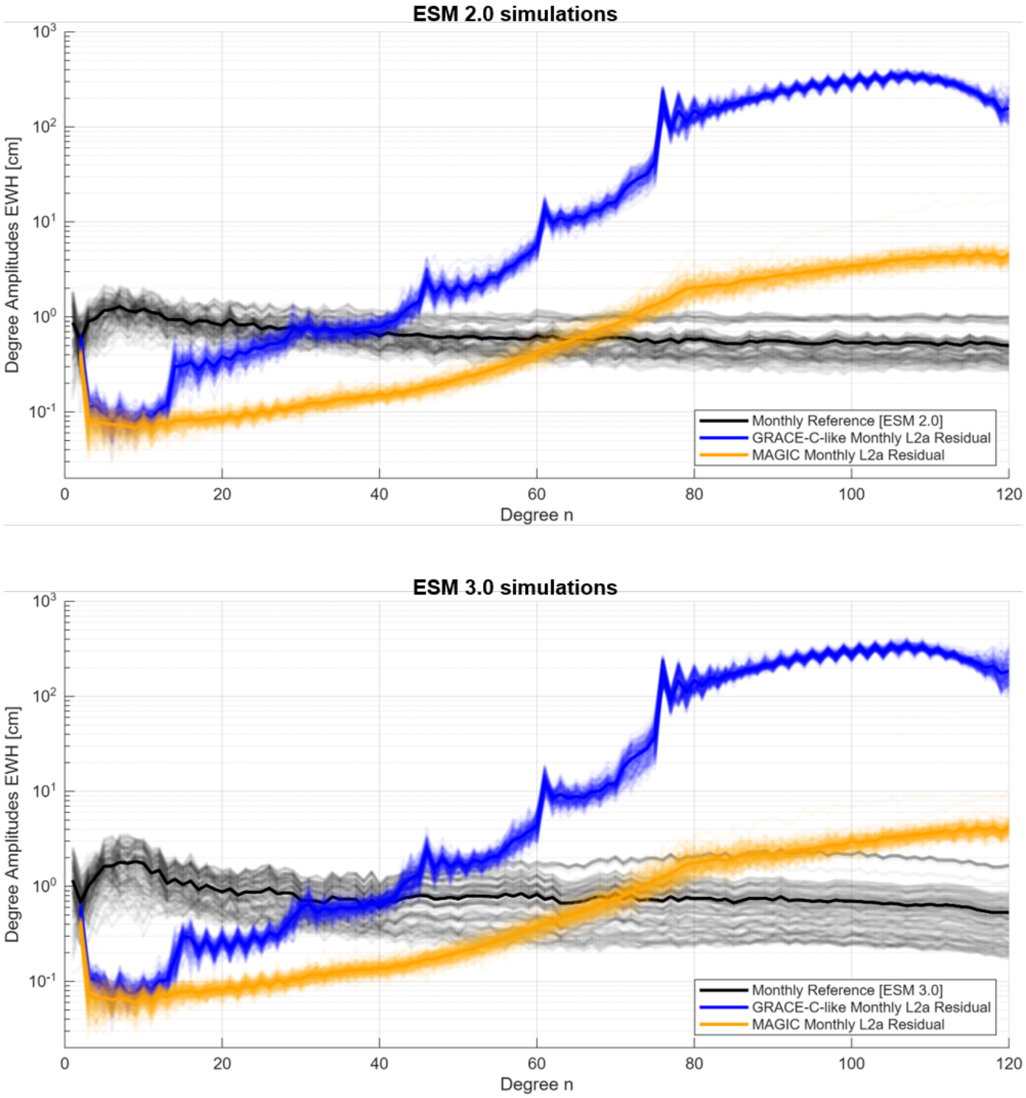

Figure 6. Degree amplitudes in cm equivalent water heights. The simulation results for ESM 2.0 are shown in the upper panel. The lower panel displays the simulation results for the ESM 3.0. In black, the mean monthly reference curve is shown. Blue denotes the mean monthly residuals of a GRACE-C-like mission, while the orange displays the mean monthly performance of a MAGIC double-pair mission. The lighter shades of the three colours display the individual monthly curves.

(Schlaak et al., 2026) we utilise the L2b data which have a Vader filter applied as well as the L2a data which we subsequently filter using a DDK3 filter. The common processing applied to both L2a and L2b to generate Level-3 (L3) products includes correction with the GIA model from the ESM and spherical harmonic synthesis up to the maximum degree 120 onto a global 1-degree grid. We then assess the variability across the 100 largest river catchments. These regions correspond to the predefined

https://doi.org/10.5194/essd-2026-576
Preprint. Discussion started: 31 August 2026

areas provided by GravIS for the TWS product (https://gravis.gfz.de/basins/rivbas/river_basins.geojson). In addition to the L3 products, we also include the H, I and B-layers from the ESM 3.0 in the comparison (downsampled to monthly resolution and 295 unfiltered).

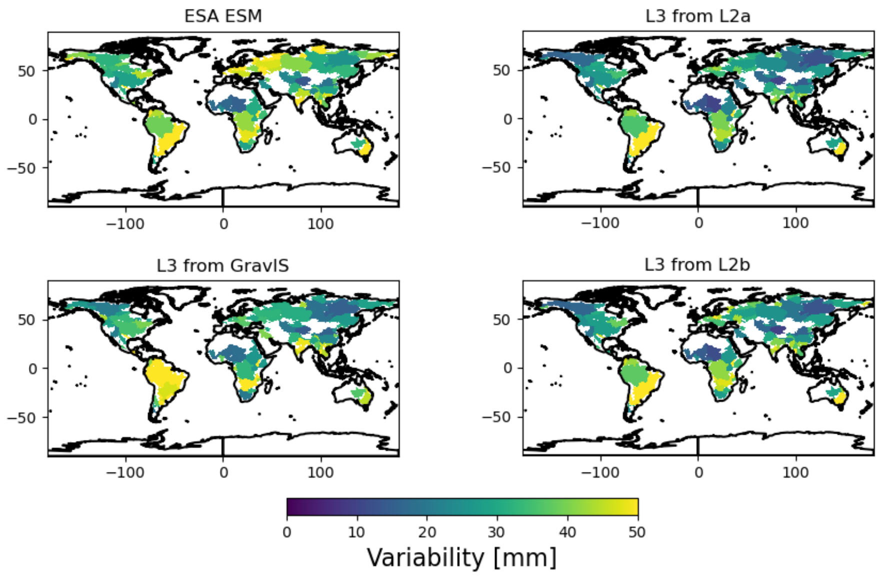

Figure 7. Root mean squared TWS signal variations after subtraction of annual, semi-annual and trend signals in TWS L3 products estimated over the period 2007 - 2020 from ESM 3.0 (top left), L2a polar pair simulations (top right), L2b polar pair simulations (bottom right) and GRACE-FO real data as available via GravIS (bottom left).

For each regional time series, we compute the RMS after removing bias, trend, annual and semi-annual components for 2007 – 2020 and show the results in Fig. 7. The overall variability is consistent across the simulation output and the GravIS data, with the largest variations in South America with an amplitude of over 50 mm EWH. There are slight discrepancies between the ESM / simulation data and GravIS TWS in e.g. Europe, eastern Russia and Alaska which are mainly confined to 300 the sub-yearly band (not-shown). However, the broadly consistent results highlight that the ESM and simulations can be used for more detailed hydrometeorologic impact studies.

As a second assessment, we focus on the ability to capture hydrometeorological extremes using the Danube River Basin as an example. For this purpose, the mean time series of all data sets is converted to z-scores, i.e., normalized on a monthly 305 basis (Zhao et al., 2017). Z-scores above 1 indicate an exceptionally high water storage, while z-scores below -1 indicate an exceptionally low water storage (Fig. 8). The Danube River Basin experienced an exceptionally snow-rich winter in 2010–2011, which is clearly reflected in the GravIS data set as well as in both the L2a and L2b simulations (Fig. 8). It is not the scope of this section to further explore the hydrometeorological relevance of this signal, but rather to demonstrate that known deviations from climatology in important European basins are indeed captured by the ESM 3.0

https://doi.org/10.5194/essd-2026-576
Preprint. Discussion started: 31 August 2026

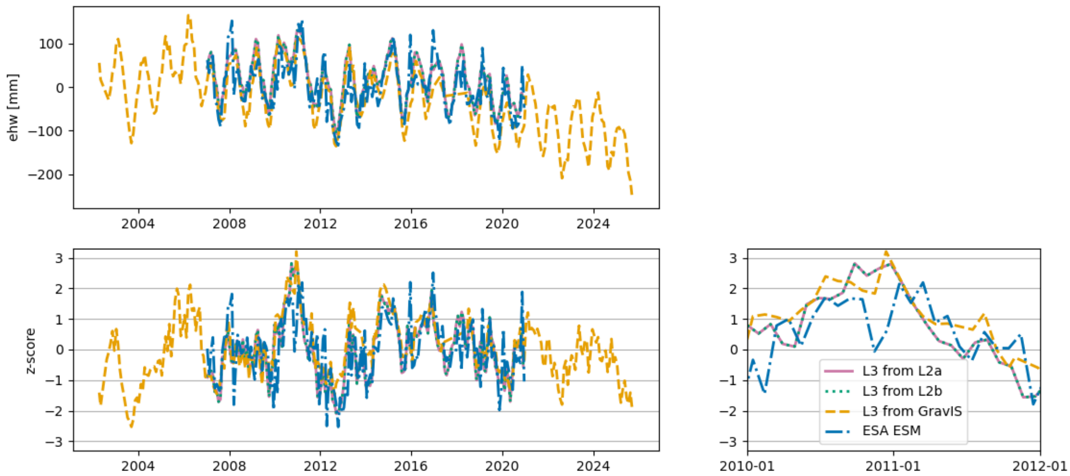

Figure 8. TWS water storage for the Danube basin (top panel) and the associated z-score indicating extreme conditions (lower left panel) with a corresponding zoom-in on the period around a major wet event during the boreal winter 2010/2011 (lower right panel).

5 Technicalities and Data Access

In order for simulation studies to be representable for a real-world mission, a number of error sources need to be included in the simulations. Importantly, the simulations need to capture the impact of temporal de-aliasing of high-frequency variations in the Earth system. Using the ESA ESM 3.0, de-aliasing can be included via the supplied error time-series labeled AOe07 which represents the errors in the atmospheric and oceanic components. The error coefficients can be added to the atmosphere and ocean layers to arrive at a realistically perturbed background model.
Additionally, we provide, and unlike ESM 2.0, an error time-series for the hydrological and cryospheric layers: HIe07. This allows for testing the impact of high-frequency hydrological changes on satellite gravimetry solutions. While its impact is expected to be smaller than for AOe07 (less variability at high frequencies) the contribution may be relevant for the increased capabilities of future multi-pair satellite missions. A dedicated publication on the preparation of the hydrological error time-series and its assessment is currently in preparation.

ESA ESM 2.0 and 3.0 cover two two consecutive time-periods and it may be useful to perform simulations for the full 26 years of the combined dataset. This is not possible, however, given the discontinuity that arises when simply concatenating both datasets. In order to allow for long-term simulations, we also provide static offsets, one for each layer in ESA ESM 2.0, that can be applied to all epochs of ESA ESM 2.0 in order to seamlessly connect the two datasets.

https://doi.org/10.5194/essd-2026-576
Preprint. Discussion started: 31 August 2026

ESA ESM 2.0 provides a single year (2006) with an increased resolution. For the updated ESM 3.0 we provide the single year 2008 with halved temporal sampling of 3 hours. This allows testing the impact of the increased variability. While all layers are provided with the increased resolution for the year, only the A, O and by consequence B layers include variability at 3-hourly frequencies. Other layers consist of linearly interpolated values from the ESMs native 6-hourly resolution. One small exception are the tsunami signals included in some epochs of the E-layer. While the post-seismic deformations of the earthquake signals in the E-layer is linearly interpolated, the tsunami signals are not interpolated but instead added as additional epochs.

The new ESA ESM 3.0 data is publicly available at GFZs Information System and Data Center (ISDC) and can be accessed via the DOI 10.5880/GFZ.UEOS.2026.001.

6 Conclusions

The updated ESA Earth System Model 3.0 representing the time-variable global gravity field for satellite simulation studies is now available. The dataset covers the years 2007 – 2020 at a 6-hourly resolution and consists of Stokes coefficients up to degree and order 180 and additionally at 3-hourly resolution for the year 2008. The model represents mass variations in the atmosphere, oceans and hydrology. It contains mass changes in the cryosphere and the deformation of the solid Earth. Additionally, the ESM includes spatially variable sea-level changes, an ensemble of 15 contemporary and historic earthquakes as well as regional mass change signals associated with changes in the Atlantic Meridional Overturning Circulation or the marine deposition of sediments from river basins.

The update of the previously existing components of the ESM includes making use of the latest ERA5 reanalysis data from ECMWF for the atmospheric component and consistently forcing the updated ocean and hydrological models. The oceanic component is processed in line with the latest release of the AOD1B de-aliasing data for the GRACE (-FO) processing but with a focus on temporal consistency. The newly used OS LISFLOOD model for the simulation of terrestrial water storage changes allows for a better representation of changes in the hydrology including groundwater abstraction and extreme events. For the cryopshere, the Greenland and Antarctic ice-sheet signals newly include long-term ice dynamics and are calibrated against GRACE (-FO) data and we extend the included glacier systems to nine individual regions from separate regional simulations. Finally, the solid Earth layer newly includes the deformation following the Little Ice Age as well as the small contributions from the core-mantle boundary.

In addition to the updated layers, the ESM 3.0 introduces three new layers. The updated A, H and I layers are so far not mass-conserving and any discharge of water into the oceans is not considered in the O-layer. Instead, we balance the mass variations in a separate B-layer by solving the sea-level equation with the A, H and I layers as input resulting in spatially heterogeneous sea-level fingerprints.

Second, we introduce a new earthquake layer E and include an ensemble of 15 earthquakes of varying magnitude including 2

https://doi.org/10.5194/essd-2026-576
Preprint. Discussion started: 31 August 2026

tsunami events. In order to allow for a long representation of the post-seismic deformations associated with the stress changes induced by the seismic events, the events are shifted towards the beginning of the time-series, mainly to 2008.
Lastly, regional target signals from the meridional deep-water transport anomalies associated with the AMOC and the trend signals from the deposition of sediments in the ocean are represented in the D-layer.

First closed-loop simulations using the new ESA ESM 3.0 and its predecessor show consistent results, indicating that the new ESM can be applied to dedicated assessments of future mission scenarios. While the new ESM shows a larger spread in the retrieved monthly degree amplitudes, these findings are in line with the greater variation in the included geophysical signals of the ESM. Comparisons between mission scenarios such as GRACE-C and MAGIC shows comparable improvements in the performance of the double-pair mission.

In summary, the updated and newly introduced layers of the ESA ESM 3.0, together with the AOe07 and HIe07 error time-series represent a comprehensive model of relevant signals for future satellite missions. While the assessments of the simulations are ongoing, the developed processing approaches will allow users to take full advantage of the new satellite observations once they become available.

7 Data availability

The ESA ESM 3.0 is publically available as:
Shihora, Linus; Klemann, Volker; Jensen, Laura; Dill, Robert; Sasgen, Ingo; Wouters, Bert; Sauber, Jeanne; Han, Shin-Chan; Tanaka, Yoshiyuki; Braitenberg, Carla; Javed, Muhammad Tahir; Maurizio, Gerardo; Lecomte, Hugo; Babeyko, Andrey; Hovius, Niels; Dobslaw, Henryk (2026): The ESA Earth System Model 3.0. GFZ Data Services. https://doi.org/10.5880/GFZ.UEOS.2026.001
Simulations based on the ESA ESM 3.0 are published as:
Schlaak, Marius; Pfeffer, Julia; Pail, Roland (2026): Simulated L2 and L3 products for impact studies of the NGGM and MAGIC gravity missions. GFZ Data Services. https://doi.org/10.5880/fidgeo.2026.049

Author contributions. Final production an processing was done by LS. Input data for the A and O layers were prepared by LS and RD. Hydrological simulations were prepared by LJ. I layer input was provided by IS and BW while S layer input was provided by VK and HL. Earthquake input was provided by JSR, SCH, YT, CB, MTJ and GM while tsunami simulations were performed by AB. D layer input was generated by LS and NH. Simulations were performed and assessed by MS and EB compared the simulated data to real world data. Original manuscript draft by LS with input from all co-authors. Project organisation and management by HD.

Competing interests. There are no competing interests.

https://doi.org/10.5194/essd-2026-576
Preprint. Discussion started: 31 August 2026

Acknowledgements. The work presented here was performed as part of the project ‚NGGM and MAGIC Science and Applications Impact Study‘, ESA Contract No. 4000145265/24/NL/SC, funded by the European Space Agency.

References

Albrecht, T., Bagge, M., and Klemann, V.: Feedback mechanisms controlling Antarctic glacial-cycle dynamics simulated with a coupled ice sheet–solid Earth model, The Cryosphere, 18, 4233–4255, https://doi.org/10.5194/tc-18-4233-2024, 2024.

Bagge, M., Klemann, V., Steinberger, B., Latinović, M., and Thomas, M.: Glacial-isostatic adjustment models using geodynamically constrained 3D Earth structures, Geochemistry Geophysics Geosystems, 22, e2021GC009 853, https://doi.org/10.1029/2021GC009853, 2021.

Balidakis, K., Sulzbach, R., Shihora, L., Dahle, C., Dill, R., and Dobslaw, H.: Atmospheric Contributions to Global Ocean Tides for Satellite Gravimetry, Journal of Advances in Modeling Earth Systems, 14, https://doi.org/10.1029/2022MS003193, 2022.

Bender, P. L., Wiese, D. N., and Nerem, R. S.: A possible Dual-GRACE mission with 90 degree and 63 degree inclination orbits, in: Proceedings of the 3rd International Symposium on Formation Flying, Missions and Technologies, pp. 1–6, ESA ESTEC, 2008.

Bingham, R. J. and Hughes, C. W.: Determining North Atlantic meridional transport variability from pressure on the western boundary: A model investigation, Journal of Geophysical Research, 113, C09 008, https://doi.org/10.1029/2007JC004679, 2008.

Boergens, E., Dobslaw, H., and Dill, R.: COST-G GravIS RL02 Continental Water Storage Anomalies, GFZ Data Services, https://doi.org/10.5880/COST-G.GRAVIS_01_L3_TWS, 2020.

Chang, L., Tang, H., Yi, S., and Sun, W.: The Trend and Seasonal Change of Sediment in the East China Sea Detected by GRACE, Geophysical Research Letters, 46, 1250–1258, https://doi.org/10.1029/2018GL081652, 2019.

Chen, J., Cazenave, A., Dahle, C., Llovel, W., Panet, I., Pfeffer, J., and Moreira, L.: Applications and Challenges of GRACE and GRACE Follow-On Satellite Gravimetry, Surveys in Geophysics, 43, 305–345, https://doi.org/10.1007/s10712-021-09685-x, 2022.

Choulga, M., Moschini, F., Mazzetti, C., Grimaldi, S., Disperati, J., Beck, H., Salamon, P., and Prudhomme, C.: Technical note: Surface fields for global environmental modelling, EGUsphere, pp. 1–30, https://doi.org/10.5194/egusphere-2023-1306, publisher: Copernicus GmbH, 2023.

Daras, I., March, G., Pail, R., Hughes, C. W., Braitenberg, C., Güntner, A., Eicker, A., Wouters, B., Heller-Kaikov, B., Pivetta, T., and Pastorutti, A.: Mass-change And Geosciences International Constellation (MAGIC) expected impact on science and applications, Geophysical Journal International, 236, 1288–1308, https://doi.org/10.1093/gji/ggad472, 2023.

Dobslaw, H., Bergmann-Wolf, I., Dill, R., Forootan, E., Klemann, V., Kusche, J., and Sasgen, I.: The updated ESA Earth System Model for future gravity mission simulation studies, Journal of Geodesy, 89, 505–513, https://doi.org/10.1007/s00190-014-0787-8, 2015.

Dobslaw, H., Bergmann-Wolf, I., Forootan, E., Dahle, C., Mayer-Gürr, T., Kusche, J., and Flechtner, F.: Modeling of present-day atmosphere and ocean non-tidal de-aliasing errors for future gravity mission simulations, Journal of Geodesy, 90, 423–436, https://doi.org/10.1007/s00190-015-0884-3, 2016.

Dumberry, M. and Mandea, M.: Gravity Variations and Ground Deformations Resulting from Core Dynamics, Surveys in Geophysics, 43, 5–39, https://doi.org/10.1007/s10712-021-09656-2, 2022.

Farrell, W. E. and Clark, J. A.: On Postglacial Sea Level, Geophysical Journal International, 46, 647–667, https://doi.org/10.1111/j.1365-246X.1976.tb01252.x, 1976.

Fettweis, X. and Grailet, J.-F.: MAR (Modèle Atmosphérique Régional) version 3.14, https://doi.org/10.5281/zenodo.13151275, regional climate model (MAR) source code including the ecRad radiation scheme; used in polar regional climate and surface mass balance simulations., 2024.

https://doi.org/10.5194/essd-2026-576
Preprint. Discussion started: 31 August 2026

Fettweis, X., Franco, B., Tedesco, M., van Angelen, J. H., Lenaerts, J. T. M., van den Broeke, M. R., and Gallée, H.: Estimating the Greenland Ice Sheet Surface Mass Balance Contribution to Future Sea Level Rise Using the Regional Atmospheric Climate Model MAR, The Cryosphere, 7, 469–489, https://doi.org/10.5194/tc-7-469-2013, 2013.

Fichefet, T. and Maqueda, M. A. M.: Sensitivity of a global sea ice model to the treatment of ice thermodynamics and dynamics, Journal of Geophysical Research: Oceans, 102, 12 609–12 646, https://doi.org/10.1029/97JC00480, 1997.

Gillet, N., Dall'Asta, F., Amblard, P. O., Claveau, R., and Aubert, J.: Waves in Earth's Core and Geomagnetic Field Forecast, Physics of the Earth and Planetary Interiors, 357, 107 284, https://doi.org/10.1016/j.pepi.2024.107284, 2024.

Greatbatch, R. J.: A note on the representation of steric sea level in models that conserve volume rather than mass, Journal of Geophysical Research: Oceans, 99, 12 767–12 771, https://doi.org/10.1029/94JC00847, 1994.

Gregory, J. M., Griffies, S. M., Hughes, C. W., Lowe, J. A., Church, J. A., Fukimori, I., Gomez, N., Kopp, R. E., Landerer, F., Cozannet, G. L., Ponte, R. M., Stammer, D., Tamisiea, M. E., and van de Wal, R. S. W.: Concepts and Terminology for Sea Level: Mean, Variability and Change, Both Local and Global, Surveys in Geophysics, 40, 1251–1289, https://doi.org/10.1007/s10712-019-09525-z, 2019.

Hagedoorn, J. M., Wolf, D., and Martinec, Z.: An estimate of global sea level rise inferred form tide gauge measurements using glacial isostatic models consistent with the relative sea level record, Pure and Applied Geophysics, 164, 791–818, https://doi.org/10.1007/s00024-007-0186-7, 2007.

Han, S.-C., Riva, R., Sauber, J., and Okal, E.: Source parameter inversion for recent great earthquakes from a decade-long observation of global gravity fields, Journal of Geophysical Research: Solid Earth, 118, 1240–1267, https://doi.org/10.1002/jgrb.50116, 2013.

Han, S.-C., Sauber, J., Broerse, T., Pollitz, F., Okal, E., Jeon, T., Seo, K.-W., and Stanaway, R.: GRACE and GRACE Follow-On Gravity Observations of Intermediate-Depth Earthquakes Contrasted With Those of Shallow Events, Journal of Geophysical Research: Solid Earth, 129, e2023JB028 362, https://doi.org/10.1029/2023JB028362, 2024.

Hersbach, H., Bell, B., Berrisford, P., Hirahara, S., Horányi, A., Muñoz-Sabater, J., Nicolas, J., Peubey, C., Radu, R., Schepers, D., Simmons, A., Soci, C., Abdalla, S., Abellan, X., Balsamo, G., Bechtold, P., Biavati, G., Bidlot, J., Bonavita, M., De Chiara, G., Dahlgren, P., Dee, D., Diamantakis, M., Dragani, R., Flemming, J., Forbes, R., Fuentes, M., Geer, A., Haimberger, L., Healy, S., Hogan, R. J., Hólm, E., Janisková, M., Keeley, S., Laloyaux, P., Lopez, P., Lupu, C., Radnoti, G., de Rosnay, P., Rozum, I., Vamborg, F., Villaume, S., and Thépaut, J.-N.: The ERA5 global reanalysis, Quarterly Journal of the Royal Meteorological Society, 146, 1999–2049, https://doi.org/10.1002/qj.3803, 2020.

Hugonnet, R., McNabb, R., Berthier, E., Menounos, B., Nuth, C., Girod, L., Fourteau, K., Bolch, T., Brun, F., Dehecq, A., Dussaillant, I., Maussion, F., Rounce, D. R., and Zemp, M.: Accelerated global glacier mass loss in the early twenty-first century, Nature, 592, 726–731, https://doi.org/10.1038/s41586-021-03436-z, 2021.

Jensen, L., Dill, R., Balidakis, K., Grimaldi, S., Salamon, P., and Dobslaw, H.: Global 0.05° water storage simulations with the OS LISFLOOD hydrological model for geodetic applications, Geophysical Journal International, 241, 1839–1851, https://doi.org/10.1093/gji/ggaf129, 2025.

Jungclaus, J. H., Fischer, N., Haak, H., Lohmann, K., Marotzke, J., Matei, D., Mikolajewicz, U., Notz, D., and von Storch, J. S.: Characteristics of the ocean simulations in the Max Planck Institute Ocean Model (MPIOM) the ocean component of the MPI-Earth system model: Mpiom CMIP5 Ocean Simulations, Journal of Advances in Modeling Earth Systems, 5, 422–446, https://doi.org/10.1002/jame.20023, 2013.

Klemann, V., Martinec, Z., and Ivins, E. R.: Glacial isostasy and plate motion, Journal of Geodynamics, 46, 95–103, https://doi.org/10.1016/j.jog.2008.04.005, 2008.

Kusche, J., Strohmenger, C., Gerdener, H., Uebbing, B., Springer, A., Ewerdwalbesloh, Y., Eicker, A., Braitenberg, C., Pastorutti, A., Pail, R., Zingerle, P., Schlaak, M., Reguzzoni, M., Rossi, L., Migliaccio, F., and Daras, I.: Benefit of MAGIC and multipair quantum satellite gravity missions in Earth science applications, Geophysical Journal International, 242, ggaf195, https://doi.org/10.1093/gji/ggaf195, 2025.

Li, Z., Zhang, Z., Scanlon, B. R., Sun, A. Y., Pan, Y., Qiao, S., Wang, H., and Jia, Q.: Combining GRACE and satellite altimetry data to detect change in sediment load to the Bohai Sea, Science of The Total Environment, 818, 151 677, https://doi.org/10.1016/j.scitotenv.2021.151677, 2022.

Madec, G., Bell, M., Blaker, A., Bricaud, C., Bruciaferri, D., Castrillo, M., Calvert, D., Chanut, J., Clementi, E., Coward, A., Epicoco, I., Ethe, C., Ganderton, J., Harle, J., Hutchinson, K., Iovino, D., Lea, D., Lovato, T., Martin, M., Martin, N., Mele, F., Martins, D., Masson, S., Mathiot, P., Mele, F., Mocavero, S., Müller, S., Nurser, A. G., Paronuzzi, S., Peltier, M., Person, R., Rousset, C., Rynders, S., Samson, G., Techene, S., Vancoppenolle, M., and Wilson, C.: NEMO Ocean Engine Reference Manual, https://doi.org/10.5281/zenodo.8167700, 2023.

Maussion, F., Butenko, A., Champollion, N., Dusch, M., Eis, J., Fourteau, K., Gregor, P., Jarosch, A. H., Landmann, J., Oesterle, F., Recinos, B., Rothenpieler, T., Vlug, A., Wild, C. T., and Marzeion, B.: The Open Global Glacier Model (OGGM) v1.1, Geoscientific Model Developments, 12, 909–931, https://doi.org/10.5194/gmd-12-909-2019, 2019.

Maussion, F., Rothenpieler, T., Dusch, M., Vlug, A., Schuster, L., Schmitt, P., Champollion, N., Marzeion, B., Li, F., Oberrauch, M., Landmann, J., Eis, J., Jarosch, A., Hanus, S., Rounce, D., Castellani, M., Bartholomew, S., Luzpaz, Merrill, C., Loibl, D., Ultee, L., Minallah, S., Thompson, S., Anton-Ub, and Gregor, P.: OGGM/oggm: v1.5.3, Zenedo, https://doi.org/10.5880/, 2022.

Meyer, U., Jäggi, A., Dahle, C., Flechtner, F., Kvas, A., Behzadpour, S., Öhlinger, F., Mayer-Gürr, T., Lemoine, J.-M., Bourgogne, S., Lasser, M., Koch, I., Flury, J., Chen, Q., Wang, C., Yan, Z., Zhou, H., and Feng, W.: International Combination Service for Time-variable Gravity Fields (COST-G) Monthly GRACE/GRACE-FO RL02 Series. V. 2.1, GFZ Data Services, https://doi.org/10.5880/COST-G.ICGEM_02_L2, 2025.

Mouyen, M., Longuevergne, L., Steer, P., Crave, A., Lemoine, J.-M., Save, H., and Robin, C.: Assessing modern river sediment discharge to the ocean using satellite gravimetry, Nature Communications, 9, 3384, https://doi.org/10.1038/s41467-018-05921-y, 2018.

Murböck, M.: Virtual Constellations of Next Generation Gravity Missions, Dissertation, Technische Universität München, München, 2015.

Nitze, I., Heidler, K., Nesterova, N., Küpper, J., Schütt, E., Hölzer, T., Barth, S., Lara, M. J., Liljedahl, A. K., and Grosse, G.: DARTS: Multi-year database of AI-detected retrogressive thaw slumps in the circum-arctic permafrost region, Scientific Data, 12, 1512, https://doi.org/10.1038/s41597-025-05810-2, 2025.

Noël, B. P. Y., van de Berg, W. J., Lhermitte, S., Wouters, B., Schaffer, N., van den Broeke, M. R., and Fettweis, X.: Six Decades of Glacial Mass Loss in the Canadian Arctic Archipelago, Journal of Geophysical Research: Earth Surface, 123, 1430–1449, https://doi.org/10.1029/2017JF004304, 2018.

Noël, B. P. Y., Jakobs, C. L., van Pelt, W. J. J., Lhermitte, S., Noël, J. P., van den Broeke, M. R., Fettweis, X., and Wouters, B.: Low Elevation of Svalbard Glaciers Drives High Mass Loss Variability, Nature Communications, 11, 4597, https://doi.org/10.1038/s41467-020-18356-1, 2020.

Noël, B. P. Y., Aðalgeirsdóttir, G., Pálsson, F., Wouters, B., Lhermitte, S., Haacker, J. M., and van den Broeke, M. R.: North Atlantic Cooling is Slowing Down Mass Loss of Icelandic Glaciers, Geophysical Research Letters, 49, e2021GL095 697, https://doi.org/10.1029/2021GL095697, 2022.

Noël, B. P. Y., Lhermitte, S., Wouters, B., and Fettweis, X.: Poleward Shift of Subtropical Highs Drives Patagonian Glacier Mass Loss, Nature Communications, 16, 3795, https://doi.org/10.1038/s41467-025-58974-1, 2025.

Pail, R., Bingham, R., Braitenberg, C., Dobslaw, H., Eicker, A., Güntner, A., Horwath, M., Ivins, E., Longuevergne, L., Panet, I., and Wouters, B.: Science and User Needs for Observing Global Mass Transport to Understand Global Change and to Benefit Society, Surveys in Geophysics, 36, 743–772, https://doi.org/10.1007/s10712-015-9348-9, 2015.

Peltier, W. R., Argus, D. F., and Drummond, R.: Space geodesy constrains ice age terminal deglaciation: The global ICE-6G_C (VM5a) model, Journal of Geophysical Research: Solid Earth, 120, 450–487, https://doi.org/10.1002/2014JB011176, 2015.

Ray, R. D.: A global ocean tide model from TOPEX/POSEIDON altimetry: GOT99. 2, National Aeronautics and Space Administration, Goddard Space Flight Center, 1999.

Roussenov, V. M., Williams, R. G., Hughes, C. W., and Bingham, R. J.: Boundary wave communication of bottom pressure and overturning changes for the North Atlantic, Journal of Geophysical Research: Oceans, 113, https://doi.org/10.1029/2007JC004501, 2008.

Sauber, J., Han, S.-C., and Loomis, B.: The Solid Earth Response to Earthquake Cycle Processes using MAGIC, https://lps25.esa.int/lps25-presentations/presentations/817/_817.pdf, eSA Living Planet Symposium 2025, 2025.

Savcenko, R., Bosch, W., Dettmering, D., and Seitz, F.: EOT11a - Global Empirical Ocean Tide model from multi-mission satellite altimetry, with links to model results, supplement to: Savcenko, Roman; Bosch, Wolfgang (2012): EOT11a - Empirical Ocean Tide Model from Multi-Mission Satellite Altimetry. Deutsches Geodätisches Forschungsinstitut (DGFI), München, 89, 49 pp, https://doi.org/10.1594/PANGAEA.834232, 2012.

Schlaak, M. and Pail, R.: Resolving climate-related mass transport trends: a parameter model comparison using closed-loop simulations of current and future satellite gravity missions, Earth, Planets and Space, 77, https://doi.org/10.1186/s40623-025-02239-0, 2025.

Schlaak, M., Pail, R., Jensen, L., and Eicker, A.: Closed loop simulations on recoverability of climate trends in next generation gravity missions, Geophysical Journal International, 232, 1083–1098, https://doi.org/10.1093/gji/ggac373, 2022.

Schlaak, M., Pfeffer, J., and Pail, R.: Simulated L2 and L3 products for impact studies of the NGGM and MAGIC gravity missions, GFZ Data Services, https://doi.org/10.5880/fidgeo.2026.049, 2026.

Shihora, L., Balidakis, K., Dill, R., Dahle, C., Ghobadi-Far, K., Bonin, J., and Dobslaw, H.: Non-Tidal Background Modeling for Satellite Gravimetry Based on Operational ECWMF and ERA5 Reanalysis Data: AOD1B RL07, Journal of Geophysical Research: Solid Earth, 127, https://doi.org/10.1029/2022JB024360, 2022a.

Shihora, L., Sulzbach, R., Dobslaw, H., and Thomas, M.: Self-attraction and loading feedback on ocean dynamics in both shallow water equations and primitive equations, Ocean Modelling, 169, 101 914, https://doi.org/10.1016/j.ocemod.2021.101914, 2022b.

Shihora, L., Liu, Z., Balidakis, K., Wilms, J., Dahle, C., Flechtner, F., Dill, R., and Dobslaw, H.: Accounting for residual errors in atmosphere–ocean background models applied in satellite gravimetry, Journal of Geodesy, 98, https://doi.org/10.1007/s00190-024-01832-7, 2024.

Shihora, L., Martin, T., Hans, A. C., Hummels, R., Schindelegger, M., and Dobslaw, H.: Relating Atlantic meridional deep-water transport to ocean bottom pressure variations as a target for satellite gravimetry missions, Ocean Science, 21, 1533–1548, https://doi.org/10.5194/os-21-1533-2025, 2025.

Steinberger, B.: Topography caused by mantle density variations: observation-based estimates and models derived from tomography and lithosphere thickness, Geophysical Journal International, 205, 604–621, https://doi.org/10.1093/gji/ggw040, 2016.

Tamisiea, M. E., Hill, E. M., Ponte, R. M., Davis, J. L., Velicogna, I., and Vinogradova, N. T.: Impact of self-attraction and loading on the annual cycle in sea level, Journal of Geophysical Research, 115, C07 004, https://doi.org/10.1029/2009JC005687, 2010.

Tu, D., Wang, H., Ren, Y., Lu, T., Bi, N., Wu, X., and Wang, A.: Modeling of the sediment transport and deposition in the Yellow River Estuary during the water-sediment regulation scheme, CATENA, 251, 108 806, https://doi.org/10.1016/j.catena.2025.108806, 2025.

https://doi.org/10.5194/essd-2026-576
Preprint. Discussion started: 31 August 2026

540 Van Der Knijff, J. M., Younis, J., and De Roo, A. P. J.: LISFLOOD: a GIS-based distributed model for river basin scale water balance and flood simulation, International Journal of Geographical Information Science, 24, 189–212, https://doi.org/10.1080/13658810802549154, 2010.

Wang, R., Heimann, S., Zhang, Y., Wang, H., and Dahm, T.: Complete synthetic seismograms based on a spherical self-gravitating Earth model with an atmosphere–ocean–mantle–core structure, Geophysical Journal International, 210, 1739–1764, 2017.

545 Zhao, M., A, G., Velicogna, I., and Kimball, J. S.: Satellite Observations of Regional Drought Severity in the Continental United States Using GRACE-Based Terrestrial Water Storage Changes, Journal of Climate, 30, 6297 – 6308, https://doi.org/10.1175/JCLI-D-16-0458.1, 2017.